ADVANCED MATERIALS INTERFACES
Open Access
www.advmatinterfaces.de

A New Mars-van Krevelen Mechanism for CO Oxidation on a Ti-Decorated MXene

Xilin Zhang, Qianqian Peng, Lu Chen, Zhansheng Lu, Zongxian Yang, and Kersti Hermansson**

First-principles computations are performed to investigate the catalytic oxidation of CO on a Ti-decorated $Cr_2TiC_2O_2$ MXene monolayer, through comprehensive analysis of charge transfer, electronic density of states, and charge density difference of the interacting systems. By comparing the reaction energy barriers, it is found that, rather than the traditional Langmuir–Hinshelwood, Eley–Rideal, and Mars-van Krevelen (MvK) mechanisms, the CO oxidation favours a new variant of the MvK mechanism, in which the anchored Ti atom activates the surface oxygen to spill over from the substrate and take part in the CO oxidation. This work highlights the importance of activating the surface oxygen atoms of MXene by foreign metal atoms to improve the catalytic activity, and suggests that further studies into the new MvK mechanism for CO oxidation may prove worthwhile.

1. Introduction

The present study focusses on the interaction and reaction of CO with a metal-decorated O-terminated MXene surface, as a model of a single-atom catalyst (SAC). MXenes have attracted enormous attention in the scientific community due to their diverse compositions, rich surface functional groups, flexible structure, superb stability, and properties.[1–3] At present, many experiments have successfully synthesized MXene and characterized the structure and properties of a range of MXenes.[4–8] MXenes have also demonstrated remarkable potential in CO oxidation reactions in recent years. Recently, Salah et al. designed $Ti_3C_2T_x$ (T_x = OH, O, and F) two-dimensional nanosheets decorated with Pd nanoparticles in the context of electrochemical CO oxidation and found significantly enhanced CO oxidation activity compare to the Pd-free nanosheets.[9] Also several theoretical studies have explored the CO oxidation reaction on MXene models, as exemplified by CO oxidation on a Ti anchoring site for Ti_2CO_2,[10] where a high activity was found, even comparable to many noble metal catalysts for low-temperature CO oxidation.

Research on MXenes is a rather new field. A search on the topic "MXene*" on Web-of-Science gives no hits before the year 2011 and over one thousand in 2022. For single-atom catalysts, a topic search on the terms ("single*atom catalyst*" or "SAC*") gives in total just a handful of hits before 2018 and over 70 publications in the year 2022. Thus this is clearly a fast-growing field but with many hurdles yet to overcome (such as system synthesizability and stability), and the field is still in many ways exploratory. Here predictions from theoretical work have an important role to play and the current paper should be seen in that light. However, it is alleviating to know that the $Cr_2TiC_2O_2$ MXene, which is the focus of the present study, has been synthesized experimentally. Among them, Liu et al.[11] successfully prepared two new MAX compounds, $(Cr_{2/3}Ti_{1/3})_3AlC_2$ and $(Cr_{5/8}Ti_{3/8})_4AlC_3$, using hot-pressing elemental powder at 1500 °C for 1 h under 30 MPa in a flowing argon atmosphere. Subsequently, Anasori et al.[12] predicted the stable existence of $Cr_2TiC_2T_x$ MXene through DFT calculation, and successfully synthesized $Cr_2TiC_2T_x$ MXene through experiments that verified the prediction of the DFT results. In particular, it has been shown that Ti atoms can be deposited on a Cr_2TiC_2 substrate by various techniques such as atomic layer deposition,[13] electrostatic adsorption,[14] pyrolysis,[15] and solution-phase[16] method; this stability of the Ti decoration was also found in a recent theoretical paper,[17] where a single Ti atom on a $Cr_2TiC_2T_x$ substrate was found to be somewhat more stable on the surface than a Ti metal cluster. These experimental and theoretical developments are the cornerstones of our research.

X. Zhang, Q. Peng, L. Chen, Z. Lu, Z. Yang
School of Physics
Henan Key Laboratory of Photovoltaic Materials
Henan Normal University
Xinxiang 453007, China
E-mail: yzx@htu.edu.cn

X. Zhang
School of Environment
Henan Normal University
Xinxiang 453007, China

K. Hermansson
Department of Chemistry–Ångström
Uppsala University
Box 538, 75121 Uppsala, Sweden
E-mail: kersti@kemi.uu.se

The ORCID identification number(s) for the author(s) of this article can be found under https://doi.org/10.1002/admi.202300070

DOI: 10.1002/admi.202300070

In addition to quantitative prediction of, e.g., energy barriers, theoretical calculations at the electronic and atomistic levels can provide unique structural and mechanistic insight exactly at the scale where catalytic chemical reaction mechanisms take place in reality. For complex materials, such as (SAC-decorated) MXenes, the trick of the trade is to use well designed model systems, which, even though they are idealized, can yield valuable scientific insight. Comparison or ranking of a range of cases where a similar computational set-up and methodology can be used is often particularly meaningful. This is the approach taken in this work where we compare and discuss four mechanisms for CO oxidation for the same substrate and with the same computational methodology.

CO oxidation is a seemingly simple reaction of great practical (environmental) value[18] as well as of fundamental importance as it is often used as a probe to examine the activity of designed catalysts.[19,20] For the CO oxidation reaction, the Eley–Rideal (ER),[21,22] and the Langmuir–Hinshelwood (LH)[23–25] mechanisms are the two standard surface mechanisms, which have been the subject of a large number of experimental and theoretical studies with the aim to determine the rate-determining reaction step (RDS) and the corresponding energy barriers for different systems and under different scenarios. For the ER mechanism, it has been shown that, due to its favorable adsorption energy, preadsorbed O_2 can be activated by an approaching CO molecule to form a CO_3 intermediate, which subsequently dissociates.[10,26] The LH mechanism involves three stages: the coadsorption of O_2 and CO molecules, the formation and dissociation of a peroxide-like (OCOO) complex intermediate, and the final desorption of CO_2.[27]

For catalysts with surface oxygen atoms available, the Mars-van Krevelen (MvK) mechanism is another possible route,[28–31] in which the surface oxygen atoms are directly involved in the catalytic reaction. This usually occurs through the reaction of a surface oxygen atom with an entering CO molecule, leaving an oxygen vacancy (V_O), which is then filled with dissociated adsorbed oxygen.[25,32] Thus, for example, Kim et al.[32] performed calculations of various CO oxidation mechanisms at the interfaces of Au nanoclusters supported on a CeO_2 surface and found that Au-CO* could be directly oxidized through the MvK mechanism by way of protruding oxygen atoms at a CeO_2-step. The low oxygen vacancy formation energy and the small activation barrier for CO_2 formation on the Au/CeO_2-step was found to yield the high CO oxidation activity and the authors of ref. [32] point out that the vacancy formation energy is a reactivity descriptor for CO oxidation. This power of the vacancy formation energy as a reactivity descriptor was further, and nicely, demonstrated by Kropp et al.[33] who compiled a "data set" of CO oxidation barriers and oxygen vacancy formation energies from literature results for density functional theory (DFT) studies of the MvK mechanism for about 20 metal oxide surfaces and metal/metal oxide interfaces. A good correlation between the two properties was found. The same linear relation might also be relevant to MXene surfaces with oxygen functional groups.

Hence, in this work, CO oxidation on Ti anchored bimetallic MXenes $Cr_2TiC_2O_2$ substrate is studied using DFT. The results will show that the MvK, ER, and LH mechanisms tend to occur in Ti-$Cr_2TiC_2O_2$ but need to overcome larger energy barriers. A new MvK mechanism different from the traditional mechanisms is proposed with a relatively smaller barrier for the rate-determining step, achieved by activating surface oxygen vacancy formation (lowering the barrier). Indeed, the vacancy formation is a key aspect of a competitive MvK mechanism, as alluded to in our brief review above of literature work on the vacancy formation energy as a descriptor of CO oxidation activity. Our computational results give that the potential barrier of the lattice oxygen dissociation from the catalyst surface is low (0.26 eV), and the reaction barrier of the rate limiting step is the smallest (0.63 eV) compared with the other mechanisms we have explored and smaller than all the other rate-determining energy barriers we have found presented in the literature for the CO oxidation on metal, metal oxide and single atom catalysts (SACs) surfaces. We suggest that the alternative new MvK mechanism is of significance to take into account in future studies of the CO oxidation reaction on MXene-based SACs.

Section 2 of this paper describes the systems and methods used in the calculations. Section 3 describes and discusses the results, starting with the bare "Ti-MXene" model (the Ti-$Cr_2TiC_2O_4$ slab) in Section 3.1, and continuing with the adsorption of O_2, CO and CO_2 on Ti-MXene (Section 3.2), and the CO oxidation reactions (Section 3.3) where the ER, LH, and two types of MvK mechanisms are presented, in that order. Section 4 gives concluding remarks.

2. Systems and Methods

Here we build a Ti-decorated SAC system of O-terminated $Cr_2TiC_2O_2$ and explore its properties by electronic structure calculations at the DFT level. Although the zero-band gap and novel magnetic properties of pristine $Cr_2TiC_2O_2$ have been widely exploited and explored,[34] its surface electronic structure and catalytic activity for CO oxidation have rarely been reported in the literature.

Our slab system is O-terminated (and subsequently Ti-decorated). It has been found inevitable that −O, −OH, and −F functional groups will adhere to the surface during the etching process of bare MXenes. It has also been shown that −OH and −F groups will be transformed into −O under the action of external potential, high temperature and water solvation, indicating that the oxygen termination is more stable.[35–37] Moreover, calculations also have shown that the −OH and −F groups are less prone to stabilize the adsorbed single metal atom than the −O terminations.[38,39]

2.1. The systems

We constructed a $Cr_2TiC_2O_2$ MXene slab (called "MXene" in the paper) with a primitive lattice constant of 2.80 Å in the x and y directions; it exhibits $P\bar{3}m1$ symmetry and is consistent with our previous study.[17] A single Ti atom was adsorbed on one side of the MXene surface. Three different adsorption sites of the Ti atom on $Cr_2TiC_2O_2$ MXene were considered; the starting sites for the ad-atom are indicated in Figure S1 (Supporting Information). The most stable adsorption site is above a Cr atom residing in the 2nd atomic layer (site 2), while adsorption above a Ti atom in the 4th atomic layer (site 3) is 0.17 eV (Table S1, Supporting

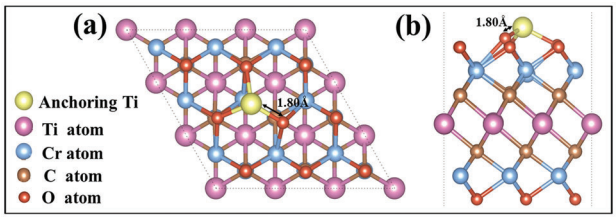

Figure 1. Top (a) and side (b) views of the stable structure of the Ti atom adsorbed on $Cr_2TiC_2O_2$ substrate.

Information) less stable. When Ti was placed above a top-layer O atom (site 1; see Figure S1), the Ti atom was found to move to site 2 and be stably adsorbed at that site after optimization. We will often refer to this adsorbed Ti atom as "Ti_{SAC}". The optimized Ti-$Cr_2TiC_2O_2$ structure (with Ti at site 2) is shown in **Figure 1** before molecular adsorption.

O_2, CO, and CO_2 molecules were adsorbed on the Ti_{SAC} side of the slab. The adsorption energy E_{ads} of adsorbates were calculated from:

$$E_{ads} = E_{total} - E_{substrate} - E_{adsorbate} \quad (1)$$

where E_{total}, $E_{substrate}$, and $E_{adsorbate}$ represent the total energy of the complex of the substrate with adsorbate, the bare substrate, and the isolated gas-phase molecule. The structures of all systems were optimized separately. The combined system will often be referred to as "'adsorbate/substrate" or variants of that. A negative value for E_{ads} signifies energetically favorable adsorption.

The energy barrier ($E_{barrier}$) is defined as $E_{barrier} = E_{TS} - E_{IS}$ and the reaction energy (ΔE) was calculated from the equation $\Delta E = E_{FS} - E_{IS}$, where E_{IS}, E_{TS} and E_{FS} are the total energies of the initial, transition and final states, respectively. According to this definition, negative ΔE values represent exothermic reactions.

2.2. Electronic Structure Calculations

Spin-polarized calculations were performed with a plane-wave basis set as implemented in the Vienna ab initio simulation package (VASP).[40,41] The electron–ion interactions were described by the projector augmented wave (PAW) method.[42,43] For chromium and oxygen, six electrons were treated as valence electrons ($3d^5 4s^1$ and $2s^2 2p^4$, respectively), and for titanium and carbon we used four electrons ($3d^2 4s^2$ and $2s^2 2p^2$ for titanium and carbon, respectively). The exchange-correlation energy was described with the generalized gradient approximation (GGA) in the form of Perdew–Burke–Ernzerhof (PBE) functional.[44] A cut-off energy of 500 eV was used for the plane wave basis set. The convergence tolerance for energy and force in geometry optimization were set to 10^{-5} eV and 10^{-2} eV/Å, respectively. The structure was described using a using (3 × 3 × 1) supercell. For the energy evaluations the Brillouin zone was sampled using a (3 × 3 × 1) Monkhorst-Pack k-point mesh. A (13 × 13 × 1) k-point grid was used for the calculation of electronic properties. The computations of the isolated molecules and atoms were performed in a cubic cell with the dimensions of 15 × 15 × 15Å^3. The DFT-D3 method was adopted to describe dispersion interactions.[45] A vacuum space of 20 Å was introduced in the z-direction to avoid the periodic interaction between the MXene slabs. In order to study the reaction paths and reaction barriers, the transition states were searched by the climbing-image nudged elastic band (CI-NEB) method,[46] using three to five images. Moreover, a harmonic vibrational analysis was performed for each transition state structure and in all cases only one virtual frequency resulted.

The electronic charge density difference (also denoted CDD) can be expressed as:

$$\Delta\rho\,(r) = \rho_{total} - \rho_{substrate} - \rho_{adsorbate} \quad (2)$$

where ρ represents the total electronic charge density of the adsorbates/substrate system, the bare substrate, and the isolated gas-phase adsorbate molecule, respectively. In Equation (2) the nuclear positions of the optimized adsorbate/substrate system are used in all three terms.

3. Results and Discussion

3.1. Before Molecular Adsorption

The bare Ti-MXene model structure in Figure 1 is our reference system. As mentioned, here the Ti atom resides at site 2 among the three discussed in Systems and Methods and it is strongly bound to the surface (E_{ads} is −7.92 eV) and distorts the top layer of the oxide, resulting in one shorter (1.80 Å) and two longer (1.92 Å) Ti–O bonds. The oxide atom forming the shorter Ti–O bond is markedly displaced from its original symmetric position on the Ti_{SAC} free surface, both laterally and "outwards" along z. Later, we will see that this atom will turn out to play a special role in one of the oxidation mechanisms that we will explore in the paper.

Furthermore, in order to explore whether the Ti atom can exist stably on the substrate, the energy difference between the adsorption energy and the cohesive energy of the Ti metal was calculated, $E_{ads} - E_{coh}$. The resulting energy difference for a Ti atom adsorbed on the surface of $Cr_2TiC_2O_2$ is −2.46 eV, suggesting that the Ti atom will be stably adsorbed on the substrate surface.

From Figure S2a (Supporting Information), we can see that when metallic titanium atoms adsorb, the highly concentrated electrons around lattice oxygen atoms and weak electron aggregation at Ti_{SAC} show the role of metallic-ionic Ti–O bond. From the difference density maps in Figure S2b (Supporting Information), we can see that Ti_{SAC} contributes electrons to its three nearest lattice oxygen atoms (blue), and a significant charge build-up is visible on the oxygen atoms around the adsorbed Ti atom (yellow). Combined with the above results, we conclude that there is strong interaction between Ti_{SAC} and the substrate, which further supports the adsorption stability of Ti_{SAC}. We also calculated the migration barrier between the most stable (site 2) and the second most stable site (site 3) which is high (0.52 eV). Using the Arrhenius equation we estimated a migration rate at room temperature of 1.7×10^4 s^{-1} (cf.[17]), which is low. The high barrier and the low migration rate support the notion that the Ti atoms are not prone to forming clusters. This is useful information, as metal dispersibility and adsorption stability on the substrate are important aspects for SACs; our results support the notion that the Ti atoms rather do not agglomerate on the substrate.

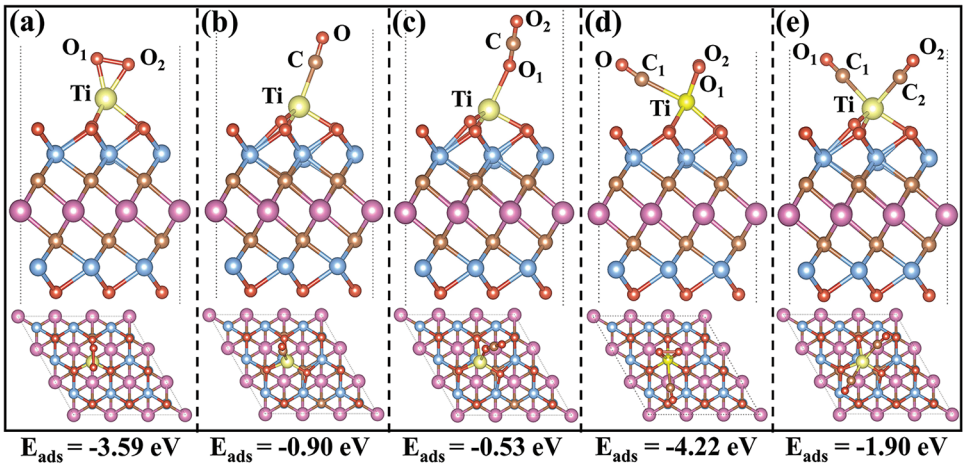

Figure 2. a–c) The optimized energetically most favorable structures of O_2, CO, and CO_2 adsorbed on Ti-anchored $Cr_2TiC_2O_2$. Top views (upper) and side view (lower) are shown. d,e) The optimized coadsorption configurations of CO + O_2, and CO + CO on Ti-$Cr_2TiC_2O_2$, respectively.

3.2. Adsorption Characters of O_2, CO, and CO_2 on Ti-Anchored $Cr_2TiC_2O_2$

The adsorption modes of the three molecular reactants (O_2, CO, and CO_2) on the Ti-MXene (i.e., Ti-$Cr_2TiC_2O_2$) substrate were analyzed first, since the capture of reactants around the active center is the first key step in the catalytic reaction. We find that each of the adsorbate molecules prefers to adsorb on the Ti atom compared to adsorption on, or nearby, a surface oxygen, indicating that the Ti atom is the active center. To search for the most energetically favorable configuration, a number of different starting configurations were tested and optimized. The most stable structures are shown in **Figure 2**a–c, together with the corresponding adsorption energies as defined by Equation (1); the adsorption energies are also given in **Table 1**. We conducted Bader charge analyses for all the adsorption configurations in Figure 2; the net atomic charges (q) and selected atomic charge changes (Δq) are given in **Table 2**.

The CO and CO_2 molecules tend to adsorb almost vertically on the catalyst surface, while O_2 lies almost horizontally. The O-O bond length increases from 1.23 Å (in the gas-phase) to 1.45 Å in Figure 2a, indicating that O_2 transforms into something akin to a peroxide ion as 1.45 Å is a typical bond length for a surface-bound O_2^{2-} species.[47] The electronic charge transferred from the substrate to the oxygen molecule (in Figure 2a) is –0.71 e, (Table 2) which is somewhat small (in magnitude) for a peroxide ion in the Bader scheme, but altogether we conclude that the adsorbed oxygen molecule essentially transforms into a peroxide ion. Upon O_2 adsorption, the one surface O atom that was significantly displaced for the bare Ti-$Cr_2TiC_2O_2$ system reverts back toward the symmetric structure of the original bare MXene system (see Figure 2 and the column labelled d(Cr-O_{latt}) in Table 1). After O_2 adsorption, the Ti–O_{latt} bond lengths all increase, i.e., the Ti–O_{latt} interactions weaken (Table 1).

Upon CO and CO_2 adsorption, the Ti-MXene structure is almost unaffected, the E_{ads} values are small and the net Bader charges of the originally neutral molecules change very little by the adsorption; see the q(mol) values in the "Ads molecule" column in Table 2. The small adsorption energy of CO_2 suggests that the release of CO_2 from the substrate is thermodynamically possible, which is conducive to the recovery of the catalyst. The magnitude of E_{ads} is seen to vary in the order O_2 >> CO > CO_2 and the magnitude of electronic charge transfer from the Ti-MXene slab to the adsorbate varies in the same way. The order for q(Ti_{SAC}) is

Table 1. Adsorption energies E_{ads} (eV) (cf. Equation (1)) and structural parameters for the various optimized systems discussed in this study (leftmost column).

System	E_{ads} [a)]	Distances within the substrate		Molecule-surface distances		Intramolecular distances	
		d(Ti-O_{latt})	d(Cr-O_{latt})	d(Ti-C)	d(Ti-O_{mol})	d(C-O_{mol})	d(O-O)
MXene	–	–	1.97, 1.97, 1.97	–	–	–	–
Ti-MXene	–	1.80, 1.92, 1.92	2.77, 2.04, 2.04	–	–	–	–
O_2/Ti-MXene	−3.59	1.97, 2.10, 1.98	2.04, 2.04, 1.98	–	1.83, 1.85	–	1.45
CO/Ti-MXene	−0.90	1.82, 1.97, 1.94	2.69, 2.00, 2.03	2.19	–	1.15	–
CO_2/Ti-MXene	−0.53	1.80, 1.94, 1.91	2.78, 2.01, 2.05	–	2.25	1.18,1.16	–
O_2+CO/Ti-MXene	−4.22	2.06, 2.02, 2.07	2.01, 2.00, 2.02	2.31	1.85, 1.85	1.13	1.45
2CO/Ti-MXene	−1.90	1.80, 2.01, 2.03	2.71, 1.99, 1.98	2.20, 2.21	–	1.15,1.15	–

MXene stands for our $Cr_2TiC_2O_2$ slab system. In all places in this table the notation Ti stands for the TiSAC atom. The atomic labels are displayed in Figure 1 by way of the colour scheme which is defined there; [a)] Per molecule for O_2, CO, and CO_2, and per 2 molecules for O_2+CO and 2CO.

Table 2. Adsorption energies E_{ads} (in eV) and atomic or molecular Bader charges q (in e units). q is the net charge of an atom or an adsorbate molecule, $\sum q$ is the sum of the net charges of a group of atoms (such as all oxygen atoms in the $Cr_2TiC_2O_2$ MXene slab or a selection of those, as indicated), Δq and $\sum \Delta q$ denote the change of the atomic charge (i.e., the magnitude and direction of the electronic charge transfer) of an atom or of a group of atoms, respectively, caused by the molecular adsorption onto the Ti-MXene slab.

System	Ads molecule		TiSAC[a]		All[b] Ti_{latt}	All[b] Cr_{latt}	All[b] O_{latt}	All[b] C_{latt}	Cr below Ti_{SAC}		3 O NNs[c] of Ti_{SAC}	
	E_{ads}	q [mol]	q(Ti)	Δq(Ti)	$\sum \Delta q$(Ti)	$\sum \Delta q$(Cr)	$\sum \Delta q$(O)	$\sum \Delta q$(C)	q(Cr)	Δq(Cr)	$\sum q$(O)	$\sum \Delta q$(O)
MXene	–	–	0	−1.61	−0.05	+0.14	+0.95	+0.57	+1.30	+0.28	−2.31	+0.55
Ti-MXene[d]	–	–	+1.61	0	0	0	0	0	+1.02	0	−2.86	0
O_2/Ti-MXene	−3.59	−0.71	+1.83	+0.22	+0.05	+0.31	+0.18	−0.05	+1.17	+0.15	−2.85	+0.01
CO/Ti-MXene	−0.90	−0.13	+1.66	+0.05	−0.02	−0.02	+0.07	+0.05	+1.07	+0.05	−2.86	0.00
CO_2/Ti-MXene	−0.53	+0.03	+1.67	+0.06	+0.01	+0.01	−0.02	−0.09	+1.03	+0.01	−2.86	0.00
O_2+CO/Ti-MXene	−4.22	CO: +0.06, O_2: −0.72	+1.83	+0.22	+0.02	+0.24	+0.09	+0.09	+1.20	+0.18	−2.86	0.00
2CO/Ti-MXene	−0.90	CO: −0.06, CO: −0.06	+1.63	+0.02	−0.02	−0.01	+0.02	+0.11	+1.08	+0.06	−2.85	+0.01

The bare Ti-MXene slab is thus the reference for the Δq values. The E_{ads} values are repeated here from Table 1 to facilitate the comparison between charge (transfer) values and adsorption strength; [a] The anchored Ti atom; [b] All atoms of this element within the MXene slab; [c] The three O atoms closest to the Ti_{SAC} atom (NN = nearest-neighbour); [d] Here all Δq values are zero as the bare Ti-MXene slab is the reference state for the Δq values on the rows below, i.e. after molecular adsorption.

O_2 >> CO ≈ CO_2, i.e., quite similar but not entirely so, which suggests that Ti is not the only donor of electron density to the adsorbed molecules. Inspection of the six columns marked "Δq" in the table helps to clarify which atoms in the Ti-MXene slab that donate electrons (electron density) to the adsorbate. As mentioned, according to the Bader scheme, the whole Ti-MXene slab transfers 0.71 electrons to the O_2 molecule transforming it into a peroxide ion. Here the Ti_{SAC} atom and the Cr atom just below the Ti_{SAC} atom are responsible for about half of the electron transfer, while many atoms in the slab contribute the remainder (all values are given in Table 2).

Here we use several additional properties to characterize the nature and trends of the molecule–surface interactions. Two such are shown in **Figure 3**: electronic density of states graphs (PDOS) and charge density difference diagram (CDD). The figure displays a significant difference between the calculated PDOS results for O_2 and CO adsorption. The Ti-3d states are strongly mixed with O_2-2p and CO-2p states near the Fermi level as seen

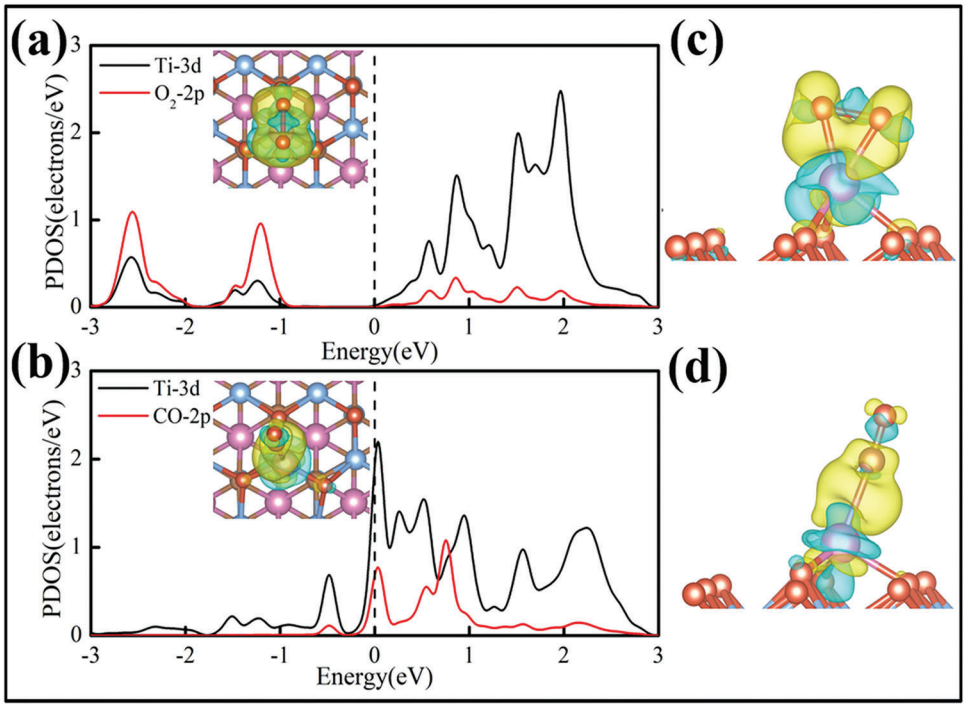

Figure 3. a,b) PDOS diagrams of O_2 and CO adsorption on the substrate, including the top view of the corresponding charge density difference (CDD, Equation (2)), while (c) and (d) are side views of the charge density difference maps of O_2 and CO adsorption on the substrate. Blue represents the loss of electron density with respect to the reference state (cf. Equation (2)) and yellow represents the gain of electrons. Dashed lines in the PDOS plots represent Fermi levels. The iso–surface level in the CDD plots is 0.003 e $Å^{-3}$ here.

from the PDOS diagrams. The CDD maps further illustrate the orbital mixing and the charge transfer. The maps in Figure 3 highlight the overall direction of electron transfer when O_2 is adsorbed: the direction is from the anchored Ti atom to O_2 and from the Cr atom. According to the Bader charge analysis in Table 2, about half of the electron transfer to O_2 originates from those two atoms. When CO is adsorbed, the CDD features are much smaller than for O_2.

As an aid toward understanding the mechanism of CO oxidation, also co–adsorption was examined. When CO and O_2 coadsorb on the Ti atom, the three nearest-neighbor surface O atoms around Ti tend to return toward their original positions on the pristine MXene surface (cf. Figure 2d,e), and, again, especially the column marked "d(Cr-O_{latt})" in Table 1). This is not the case when two CO molecules co–adsorb. The energies for co–adsorption are given in the figure (and in Table 1) and indicate that co–adsorption of CO and O_2 is less stable that the sum of their respective adsorption energies. In the case of an extended surface containing several dispersed Ti_{SAC} sites, co–adsorption would thus be less likely than "individual adsorption," an the LH mechanism would be less prone to occur. In Section 3.3, we will examine the above conjecture concerning the LH mechanism, along with other mechanisms, in a systematic fashion. Figure 2 also displays the optimized structure and energy for co–adsorption of two CO molecules; this constellation is slightly more stable than isolated species adsorption. However, since the adsorption of O_2 is much stronger than that of CO, the co–adsorption of the two CO is not preferable, hence the TER mechanism will not be discussed in detail in the following.

3.3. CO Oxidation on Ti-$Cr_2TiC_2O_2$

In this section we will focus on the bi-molecular LH and ER mechanisms and on two versions of MvK mechanism: the traditional one and a new alternative variant that we present. As mentioned, we also considered the ter-molecular Eley–Rideal (TER) mechanism but did not deem it feasible, given that it requires two CO molecules to co–adsorb on the substrate in the presence of oxygen.

Energy barriers were derived from NEB calculations as mentioned in the Systems and Methods section. We find that the potential energy barrier in the traditional MvK mechanism, where CO reacts directly with lattice oxygen to produce CO_2, is quite high (0.92 eV) and we will instead propose an alternative MvK mechanism, where the anchored Ti atom promotes CO oxidation by first activating a surface oxygen (O_{latt}) to displace onto the surface with a rather low rate limiting barrier; this turns out to be the best reaction path among the four that we consider. In the following we will often denote a surface-bound molecule with an asterisk (*). Detailed data are given in Tables S2–S15 (Supporting Information).

3.3.1. ER Mechanism

Here the first step is to break the O–O bond of a pre–adsorbed O_2 molecule (peroxide species) by the adsorption of CO. Let us first study the O–O bond breaking of O_2* in the absence of CO (**Figure 4**). In the **TS** state, the O–O bond length extends from 1.45 to 1.94 Å, with a barrier of 0.80 eV. The large barrier and the endothermic process (+0.35 eV) indicate that the O–O bond scission is not easy, which suggests that the ER mechanism will not be a preferred mechanism. In the following we will test this hypothesis.

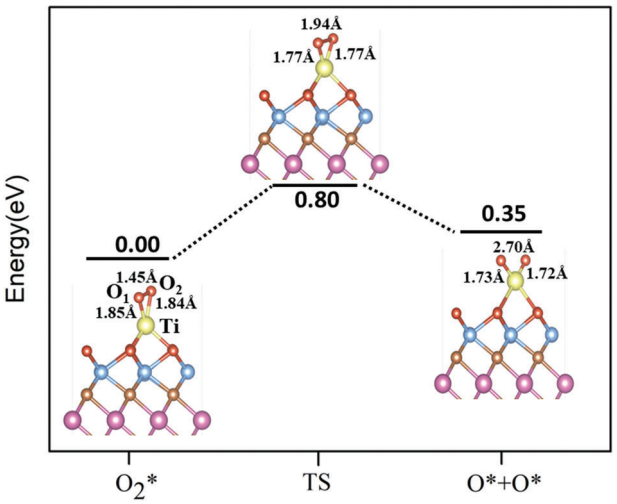

Figure 4. The dissociation mechanism of O_2 absorbed on Ti-$Cr_2TiC_2O_2$ in the Eley–Rideal (ER) mechanism.

Now let us thus add a CO molecule. The whole process of the ER mechanism is reported in **Figure 5**, where the O_2 molecule is pre–adsorbed on the active site (the Ti_{SAC} atom) in the initial state (CO + O_2*), then CO approaches and forms an intermediate state (**TS1**) including a dissociated O_2 and a physically adsorbed CO, instead of the usually formed CO_3.[10,48] This intermediate can easily transform into CO_2 and an O atom (O*+OCO*) by overcoming an energy barrier of 0.31 eV. The key geometric parameters and energy barriers of each state are listed in Tables S4 and S5 (Supporting Information). At **TS1**, d(O_1–O_2) is stretched to 2.75 Å from 1.45 Å in the initial state, indicating that the O–O bond has completely broken and that the adsorption of CO here promotes the dissociation of O_2. Then, via the O*+OCO* intermediate to the final state (O*+CO_2), the first CO_2 is produced, with an endothermic heat of +0.48 eV (Figure 5). As can be seen from Figure 5, the distance between the CO_2 and the Ti_{SAC} is as high as 3.34 Å, which indicates that there is almost no interaction between the product and the catalyst. At the same time, the calculated adsorption energy of the product CO_2 is −0.01 eV, i.e. very small, which is consistent with the previous analysis. The weak interaction indicates that the first CO_2 product is readily desorbed spontaneously from the substrate surface.

Next, we consider a second CO molecule approaching the remaining O* atom to form a second CO_2 molecule (right-hand panel of Figure 5). At **TS2**, the C–O bond length has contracted from 3.04 to 1.64 Å, accompanied by a very high energy barrier (0.95 eV) and the whole process is exothermic by −0.50 eV. The high energy barrier indicates that this process is kinetically unfavorable, which may be attributed to the strong interaction between the remaining Ti-anchored O

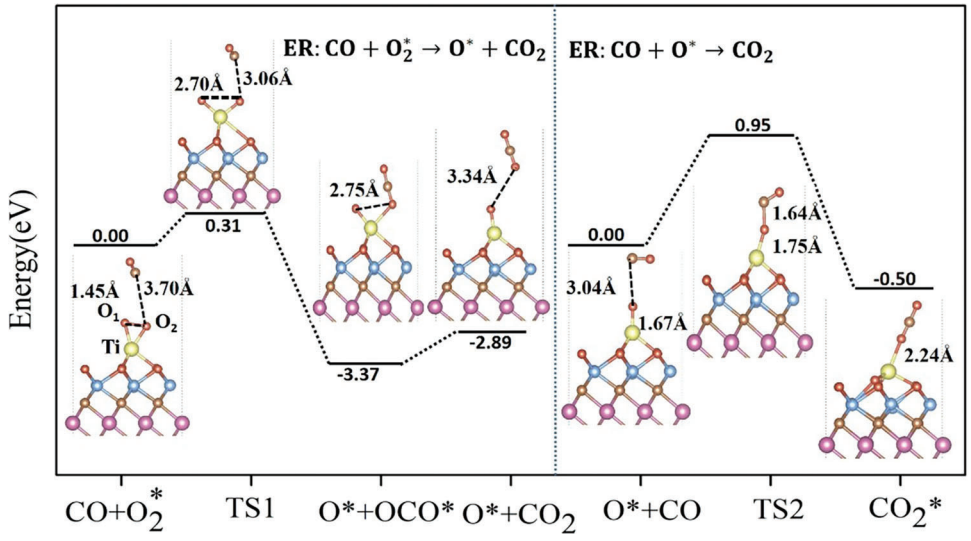

Figure 5. The reaction pathway of CO oxidation on the Ti-anchored $Cr_2TiC_2O_2$ monolayer via the Eley–Rideal (ER) mechanism.

atom and the substrate. Moreover, the adsorption energy of this CO_2 molecule is relatively small (Table 1), indicating easy desorption.

The results show that it is the formation of the second CO_2 molecule that is the rate limiting step of the ER mechanism on our $Cr_2TiC_2O_2$ slab with a barrier of 0.95 eV. This high value suggests that the ER mechanism on Ti-MXene is larger than ER barriers found for CO oxidation on some other non–noble metal SAC atoms such as Ti/Ti_2CO_2 (0.23 eV),[10] Zn/Mo_2CO_2 (0.15 eV),[23] and Co_1/Mo_2CS_2 (0.88 eV).[49]

3.3.2. LH Mechanism

Here the most energetically favorable co–adsorption configuration of CO and O_2 was taken as the initial state, as depicted in **Figure 6** together with the reaction pathway and its associated energies and selected geometrical parameters. The O–O bond in the **TS** extends from 1.45 to 2.71 Å and the molecule displaces to a symmetric position with respect to the CO group. In the pathway

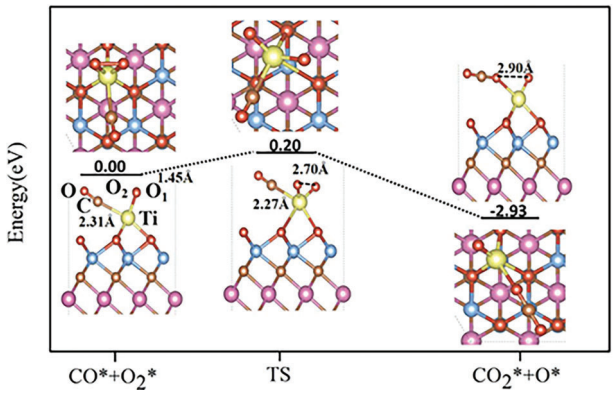

Figure 6. The reaction pathway of the first CO_2 molecular generation on the Ti-anchored $Cr_2TiC_2O_2$ monolayer via the Langmuir–Hinshelwood (LH) mechanism.

from the TS to the final state, one of the two oxygen atoms develops a bond with the co–adsorbed CO molecule to form the first CO_2 molecule. The reaction barrier is 0.20 eV and the exothermic heat is −2.93 eV. The adsorption energy of the product CO_2 is calculated to be −0.65 eV, i.e. the desorption energy is +0.65 eV. On the whole, a large amount of heat is released during the whole process of the LH mechanism, which is sufficient to desorb CO_2 from the catalyst surface.

After desorption of the CO_2 molecule to the gas-phase, a second CO molecule was made to approach the remaining O atom to form the second CO_2 molecule, creating the same scenario as that in the right-hand panel of the ER mechanism in Figure 5. Again, due to its high reaction barrier (0.95 eV), this process acts as the rate-limiting step and hinders the realization of the LH mechanism.

3.3.3. MvK Mechanisms

In the traditional MvK mechanism, an adsorbed CO molecule reacts directly with a lattice oxygen on the catalyst surface to form CO_2, which subsequently desorbs, leaving an oxygen vacancy. The reaction of the adsorbed CO with the surface lattice oxygen atoms to form CO_2 is often considered to be a rate-limiting step, making the discussion of the subsequent steps (such as surface recovery reactions) less relevant. As shown in **Figure 7**, also in our case the CO* + O_{latt} reaction step has a high barrier (0.92 eV) and the step is an endothermic process (+0.89 eV); thus the traditional MvK mechanism is not likely to be realized on $Ti\text{-}Cr_2TiC_2O_2$ from the perspective of both thermodynamics and kinetics.

Here instead we propose a new, alternative MvK mechanism. First, a surface oxygen atom is spilled over from the MXene surface to the Ti_{SAC} atom, forming an oxygen vacancy (O_v) in the substrate and a bound oxygen on Ti_{SAC} (O*) in the process (**Figure 8**, left panel). The oxygen atom shown in green (O*) is the one which has spilled over from the lattice by overcoming a barrier of 0.26 eV to attach to the Ti anchor atom. After allowing the

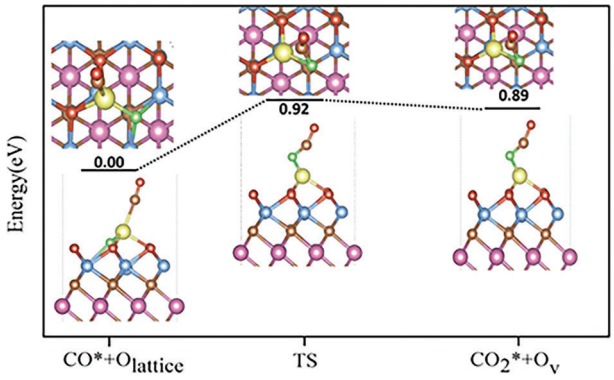

Figure 7. The reaction pathway of the first CO_2 molecular generation on the Ti-anchored $Cr_2TiC_2O_2$ monolayer via the traditional MvK mechanism. The green-colored oxygen atom is the one in the $Cr_2TiC_2O_2$ MXene lattice which finally becomes incorporated into the CO_2 molecule.

Ti_{SAC}, O* and O_v atoms to find their optimal mutual arrangement we let a CO molecule adsorb and react with the O-decorated Ti-atom to form a CO_2* molecule (Figure 8, right panel) by overcoming a potential barrier of 0.56 eV (**TS2**). The adsorption energy of the product CO_2 on the substrate was calculated as −0.58 eV; this relatively weak adsorption energy indicates that the first product CO_2 could be desorbed from the substrate surface.

After the desorption of CO_2 produced by the process in Figure 8, an oxygen vacancy is left on the catalyst surface. The stable adsorption position of the Ti_{SAC} on the current structure ($Cr_2TiC_2O_2$ structure with an oxygen vacancy) was examined, and its most stable adsorption configuration is the **FS** state in Figure S4 (Supporting Information). As shown in Figure S4 (Supporting Information), we examined the transition barrier of the Ti_{SAC} migrating from the adsorption position after CO_2 desorption to the most stable position (FS state)). The results show that the Ti migration has an energy barrier of only 0.30 eV, indicating that the **FS** state in Figure S4 (Supporting Information) is likely able to serve as the initial state of the second CO_2 molecule generation process.

As for the subsequent reaction process, according to previous studies, there are two alternative ways that correspond to the recovery ways of the two catalysts respectively in the traditional MVK mechanisms, namely:[50] (1) an adsorbed O_2 fills the oxygen vacancy, leaving an oxygen atom exposed on the surface, and the second CO molecule reacts with the oxygen atom to generate CO_2, which is then desorbed. Finally, the catalyst is refreshed and ready for a new round of CO oxidation; (2) a second CO molecule reacts with a second surface lattice oxygen atom to produce CO_2, which then desorbs, giving two oxygen vacancies, which are then filled by an O_2 molecule, making the catalyst refreshed.

First of all, for the (1) reaction pathway, we find by structural optimization that the O_2 molecule adsorbs onto the Ti atom rather than fills the oxygen vacancy, inferring that the activity of the metal Ti atom toward O_2 is high also in the presence of an oxygen vacancy. Therefore, the (1) reaction pathway mentioned earlier in the traditional MvK mechanism is not feasible in the system we studied.

Instead, the second reaction pathway is examined here. As shown in **Figure 9**, a lattice oxygen at the surface next to the Ti atom in the initial state is likely prone to escape from the substrate surface with a small reaction barrier of 0.31 eV to reach the final state (as shown in Figure 9, left panel). In this process, the Ti–O bond contracts slightly (from 1.80 to 1.67 Å). Then the second CO molecule reacts with the oxygen atom (O*), creating a second CO_2 molecule and a second O vacancy by overcoming an energy barrier of 0.63 eV, as shown in Figure 9 (right panel).

Finally the catalyst is re–oxidized to make the catalyst refreshed. As shown in **Figure 10**, an O_2 molecule is then first adsorbed into one oxygen vacancy, and then dissociated with the top oxygen atom migrating to the other vacancy, completing the oxidation process. The transition state barrier is 0.46 eV, indicating

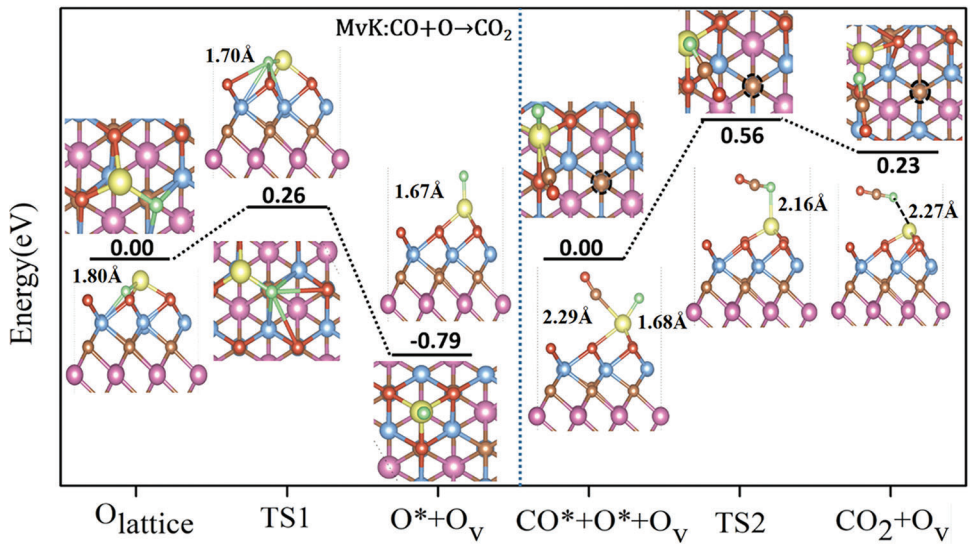

Figure 8. The reaction pathway of the first CO_2 molecule on the Ti-anchored $Cr_2TiC_2O_2$ monolayer via the new MvK mechanism. The dotted ring in each top-view image in the second part of the figure represents the oxygen vacancy. The green-colored oxygen atom is the one in the $Cr_2TiC_2O_2$ MXene lattice and finally become incorporated into the CO_2 molecule.

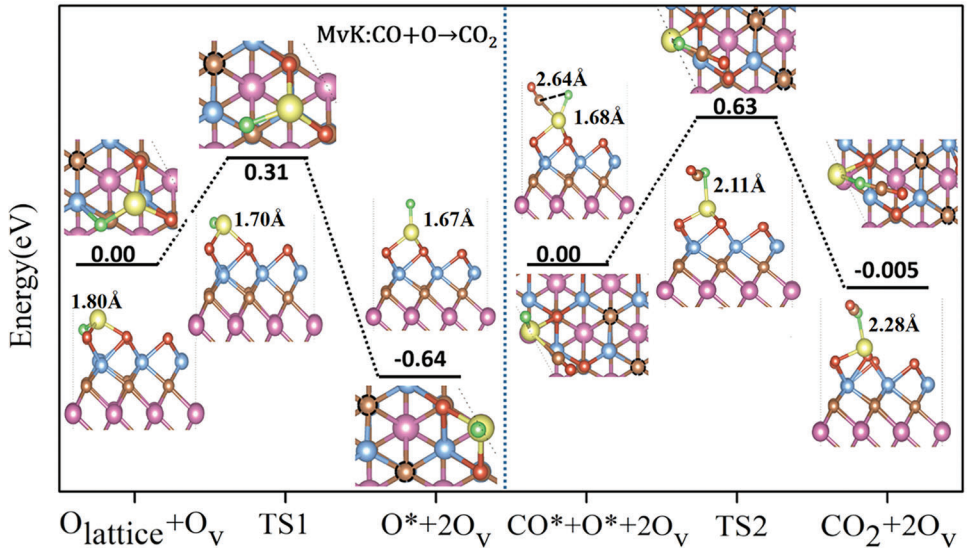

Figure 9. The reaction pathway for generation of the second CO_2 molecule on the Ti-anchored $Cr_2TiC_2O_2$ monolayer via the new MvK mechanism. The position of the dotted rings represents the oxygen vacancy. The green-colored oxygen atom is the one in the $Cr_2TiC_2O_2$ MXene lattice which finally becomes incorporated into the CO_2 molecule.

that the catalyst recovery is also convenient. To sum up the above results, our modified MvK mechanism where the lattice oxygen, turned into O*, reacts with the CO* molecule using the Ti_{SAC} atom as the "reactor vessel" seems promising as its rate-limiting step barrier (0.63 eV) is lower than others pathways in our work (ER, LH, and traditional MvK mechanism). In summary, the alternative MvK mechanism may be of significance in the understanding of the functionality of metal-based SAC MXenes and the development of CO oxidation mechanisms.

4. Discussion and Concluding Remarks

We have discussed four potential candidate reaction mechanisms for CO oxidation on a model $Cr_2TiC_2O_2$ MXene surface, decorated with a single Ti atom (Ti_{SAC}). Out of these we found a favorable mechanism in the form of an MvK variant in which at each Ti_{SAC}, two lattice oxygen atoms spill over from the substrate surface to the metal atom by forming oxygen vacancies with the assistance of the adsorbed Ti atom; the O atoms then react and proceed to the CO oxidation. The surface vacancies can be restored by dissociating an O_2 molecule at vacancies with a low barrier of 0.46 eV. The rate-limiting step of this new MvK mechanism has a lower barrier (+0.63 eV) than the ER and LH mechanisms (both +0.95 eV) and the traditional MvK mechanism (+0.92 eV). Moreover, our study shows that oxygen vacancies are easy to generate on Ti-decorated $Cr_2TiC_2O_2$. Both these types of mechanistic information can provide valuable theoretical guidance for efficient optimization of CO oxidation in proton exchange membrane fuel cells. Furthermore, our results demonstrate that the Ti-$Cr_2TiC_2O_2$ structure could be a promising catalyst for CO oxidation without the participation of any precious metals.

In recent years, reaction mechanisms and catalytic activity of CO oxidation have been studied extensively. **Table 3** shows the rate-limiting steps and corresponding barriers for different systems for CO oxidation reactions obtained from DFT calculations. Xu et al. proposed that Pd atom adsorbed on MgO substrate with

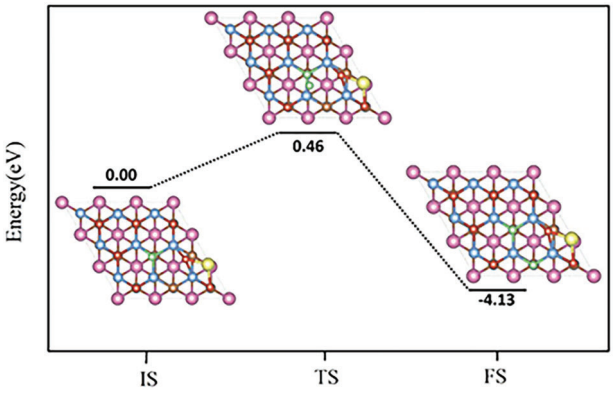

Figure 10. The energy barrier for the re-oxidation reaction of the reduced catalyst via an O_2 molecule, which adsorbs in the vacancy and subsequenty dissociates. Green atoms represent the filled O_2 molecules.

Table 3. The rate-limiting steps and barriers of different systems for CO oxidation reaction obtained from some DFT studies in the literature and our work.

Systems	Rate limiting steps	Barriers [eV]	Ref.
Pd/Fs-defect MgO	$CO+O_2 \rightarrow OOCO$	1.28	[25]
Pt (111)	$CO+O \rightarrow CO_2$	1.05	[51]
Ni/MgO	$CO+O_2 \rightarrow OOCO$	0.97	[25]
Pd (111)	$CO+O \rightarrow CO_2$	0.91	[52]
Au/ZrO_2	$CO+O \rightarrow CO_2$	0.81	[53]
Pt_1/FeO_x	$CO+O \rightarrow CO_2$	0.79	[54]
$Ti/Cr_2TiC_2O_2$	$CO+O \rightarrow CO_2$	0.63	Present work

oxygen vacancy could be used as the catalyst for CO oxidation, and the rate-limiting step (+1.28 eV) was found to be the generation of an OOCO* intermediate from the co–adsorption of CO and O_2,[25] Zhang et al. reported that the rate-determining step for CO oxidation on Pd (111) is also the combination of oxygen atom and CO, and the barrier is 0.91 eV.[52] Liang et al. found that the catalytic cycle of SAC Pt_1/FeO_x is much easier than that of Fe_1/FeO_x, because the activation energy of CO+O→CO_2 on Pt_1/FeO_x (0.79 eV) is lower than that on Fe_1/FeO_x (1.09 eV).[54] Compared with previous researches, we can conclude that the proposed single-atom model catalyst (Ti-$Cr_2TiC_2O_2$) and its new MvK mechanism provide a competitive candidate system for CO oxidation.

Supporting Information

Supporting Information is available from the Wiley Online Library or from the author.

Acknowledgements

This work was financially supported by the National Natural Science Foundation of China (Nos. 11874141, 11904084, and U2004212), the Henan Overseas Expertise Introduction Center for Discipline Innovation (CXJD2019005), the China Postdoctoral Science Foundation (2021M690933), the Swedish Research Council (VR), and the Swedish National Strategic e-Science program eSSENCE. The simulations were performed on resources provided by the High Performance Computing Center of Henan Normal University.

Conflict of Interest

The authors declare no conflict of interest.

Data Availability Statement

The data that support the findings of this study are available from the corresponding author upon reasonable request.

Keywords

activating surface oxygen, CO oxidation, MXene, new Mars-van Krevelen mechanism, single atom catalyst (SAC)

Received: February 6, 2023
Revised: April 7, 2023
Published online: August 10, 2023

[1] M. Naguib, M. Kurtoglu, V. Presser, J. Lu, J. Niu, M. Heon, L. Hultman, Y. Gogotsi, M. W. Barsoum, *Adv. Mater.* **2011**, *23*, 4248.
[2] K. R. G. Lim, A. D. Handoko, S. K. Nemani, B. Wyatt, H. Jiang, J. Tang, B. Anasori, Z. W. Seh, *ACS Nano* **2020**, *14*, 10834.
[3] Y. Gogotsi, B. Anasori, *ACS Nano* **2019**, *13*, 8491.
[4] M. S. Bhargava Reddy, S. Kailasa, B. C. G. Marupalli, K. K. Sadasivuni, S. Aich, *ACS Sens.* **2022**, *7*, 2132.
[5] X. Jiang, A. V. Kuklin, A. Baev, Y. Ge, H. Ågren, H. Zhang, P. N. Prasad, *Phys. Rep.* **2020**, *848*, 1.
[6] S. Venkateshalu, G. M. Tomboc, B. Kim, J. Li, K. Lee, *ChemNanoMat* **2022**, *8*, 202200320.
[7] C. J. Zhang, Y. Ma, X. Zhang, S. Abdolhosseinzadeh, H. Sheng, W. Lan, A. Pakdel, J. Heier, F. Nüesch, *Energy Environ. Mater.* **2020**, *3*, 29.
[8] P. Huang, W. Han, *Nano-Micro Lett.* **2023**, *15*, 68.
[9] B. Salah, K. Eid, A. M. Abdelgwad, Y. Ibrahim, A. M. Abdullah, M. K. Hassan, K. I. Ozoemena, *Electroanalysis* **2022**, *34*, 677.
[10] X. Zhang, J. Lei, D. Wu, X. Zhao, Y. Jing, Z. Zhou, *J. Mater. Chem. A* **2016**, *4*, 4871.
[11] Z. Liu, L. Zheng, L. Sun, Y. Qian, J. Wang, M. Li, *J. Am. Ceram. Soc.* **2014**, *97*, 67.
[12] B. Anasori, Y. Xie, M. Beidaghi, J. Lu, B. C. Hosler, L. Hultman, P. R. C. Kent, Y. Gogotsi, M. W. Barsoum, *ACS Nano* **2015**, *9*, 9507.
[13] X. Zhang, B. Shao, Z. Sun, Z. Gao, Y. Qin, C. Zhang, F. Cui, X. Yang, *Ind. Eng. Chem. Res.* **2020**, *59*, 1822.
[14] J. Wang, X. Wei, X. Wang, W. Song, W. Zhong, M. Wang, J. Ju, Y. Tang, *Inorg. Chem.* **2021**, *60*, 5890.
[15] C. Wen, T. Zhu, X. Li, H. Li, X. Huang, G. Sun, *Chin. Chem. Lett.* **2020**, *31*, 1000.
[16] H. Chen, N. Chen, M. Zhang, M. Li, Y. Gao, C. Wang, G. Chen, F. Du, *Nanotechnology* **2019**, *30*, 134001.
[17] X. Zhang, L. Chen, Q. Sun, Y. Pang, X. Yang, Z. Yang, *Int. J. Hydrogen Energy* **2021**, *46*, 25457.
[18] L. A. Lozano, B. M. C. Faroldi, M. A. Ulla, J. M. Zamaro, *Nanomaterials* **2020**, *10*, 165.
[19] H. Freund, G. Meijer, M. Scheffler, R. Schlögl, M. Wolf, *Angew. Chem., Int. Ed.* **2011**, *50*, 10064.
[20] C. Rossignol, S. Arrii, F. Morfin, L. Piccolo, V. Caps, J. Rousset, *J. Catal.* **2005**, *230*, 476.
[21] W. H. Weinberg, *Acc. Chem. Res.* **1996**, *29*, 479.
[22] S. Sinthika, S. T. Vala, Y. Kawazoe, R. Thapa, *ACS Appl. Mater. Interfaces* **2016**, *8*, 5290.
[23] C. Cheng, X. Zhang, Z. Yang, K. Hermansson, *Adv. Theory Simul.* **2019**, *2*, 1900006.
[24] S. Ali, Z. Xie, H. Xu, *ChemPhysChem* **2021**, *22*, 2352.
[25] H. Xu, C. Xu, D. Cheng, J. Li, *Catal. Sci. Technol.* **2017**, *7*, 5860.
[26] C. Cheng, X. Zhang, Z. Yang, Z. Zhou, *ACS Appl. Mater. Interfaces* **2018**, *10*, 32903.
[27] J. C. González-Torres, V. Bertin, E. Poulain, O. Olvera-Neria, *J. Mol. Model.* **2015**, *21*, 279.
[28] F. Li, L. Li, X. Liu, X. Z. Liu, Z. Chen, *J. Subst. Abuse Treat.* **2016**, *17*, 3170.
[29] H. Y. Kim, G. Henkelman, *J. Phys. Chem. Lett.* **2012**, *3*, 2194.
[30] C. Wang, X. Gu, H. Yan, Y. Lin, J. Li, D. Liu, W. Li, J. Lu, *ACS Catal.* **2017**, *7*, 887.
[31] P. Mars, D. W. van Krevelen, *Chem. Eng. Sci.* **1954**, *3*, 41.
[32] H. Y. Kim, G. Henkelman, *J. Phys. Chem. Lett.* **2013**, *4*, 216.
[33] T. Kropp, M. Mavrikakis, *J. Catal.* **2019**, *377*, 577.
[34] J. Yang, X. Zhou, X. Luo, S. Zhang, L. Chen, *Appl. Phys. Lett.* **2016**, *109*, 203109.
[35] Y. Zhang, X. Zhang, C. Cheng, Z. Yang, *Chin. Chem. Lett.* **2020**, *31*, 931.
[36] C. Ling, L. Shi, Y. Ouyang, J. Wang, *Chem. Mater.* **2016**, *28*, 9026.
[37] Z. W. Seh, K. D. Fredrickson, B. Anasori, J. Kibsgaard, A. L. Strickler, M. R. Lukatskaya, Y. Gogotsi, T. F. Jaramillo, A. Vojvodic, *ACS Energy Lett.* **2016**, *1*, 589.
[38] D. Kan, D. Wang, Y. Wei, *J. Mater. Chem. A* **2020**, *8*, 3097.
[39] X. Zhang, C. Xu, Y. Zhang, C. Cheng, Z. Yang, K. Hermansson, *Int. J. Hydrogen Energy* **2021**, *46*, 8477.
[40] G. Kresse, J. Furthmüller, *Phys. Rev. B* **1996**, *54*, 11169.
[41] G. Kresse, J. Furthmüller, *Comp. Mater. Sci.* **1996**, *6*, 15.

[42] G. Kresse, D. Joubert, *Phys. Rev. B* **1999**, *59*, 1758.
[43] P. E. Blöchl, *Phys. Rev. B* **1994**, *24*, 17953.
[44] J. P. Perdew, K. Burke, M. Ernzerhof, *Phys. Rev. Lett.* **1996**, *77*, 3865.
[45] S. Grimme, S. Ehrlich, L. Goerigk, *J. Comput. Chem.* **2011**, *32*, 1456.
[46] G. Henkelman, B. P. Uberuaga, H. Jónsson, *J. Chem. Phys.* **2000**, *113*, 9901.
[47] P. A. Gravil, D. M. Bird, J. A. White, *Phys. Rev. Lett.* **1996**, *77*, 3933.
[48] Q. Jiang, J. Zhang, Z. Ao, H. Huang, H. He, Y. Wu, *Front Chem* **2018**, *6*.
[49] S. H. Talib, S. Baskaran, X. Yu, Q. Yu, B. Bashir, S. Muhammad, S. Hussain, X. Chen, J. Li, *Sci. China Mater.* **2021**, *64*, 651.
[50] B. Liu, W. Li, W. Song, J. Liu, *Phys. Chem. Chem. Phys.* **2018**, *20*, 16045.
[51] A. Alavi, P. Hu, T. Deutsch, P. L. Silvestrelli, J. Hutter, *Phys. Rev. Lett.* **1998**, *80*, 3650.
[52] C. J. Zhang, P. Hu, *J. Am. Chem. Soc.* **2001**, *123*, 1166.
[53] A. R. Puigdollers, G. Pacchioni, *ChemCatChem* **2017**, 1119.
[54] J. Liang, X. Yang, C. Xu, T. Zhang, J. Li, *Chin. J. Catal.* **2017**, *38*, 1566.